DE GRUYTER Z. Phys. Chem. 2014; Galley Proof

Oliver H. Seeck*

X-ray Reflectometry and Related Surface Near X-ray Scattering Methods

Abstract: Surface sensitive X-ray scattering methods are mostly non-destructive tools which are frequently used to investigate the nature of thin films, interfaces and artificial near surface structures. Discussed here are diffraction based methods, namely reflectometry and the related techniques grazing incidence diffraction and crystal truncation rod measurements. For the experiment, an X-ray beam is diffracted from surface near structures of the sample and detected by adequate detectors. To analyze the data the according X-ray scattering theory has to be applied. The full theory of surface sensitive X-ray scattering is complex and based on general considerations from wave optics. However, instructive insights into the scattering processes are provided by the Born-approximation which in many cases yields sufficient results. The methods are applied to solve the structure of a mercury-electrolyte interface during a chemical reaction and to determine the strain distribution in surface near SiGe quantum dots.

Keywords: X-ray Reflectivity, X-ray Surface Diffraction, Crystal Truncation Rods, Structure of Surfaces and Interfaces.

DOI 10.1515/zpch-2014-0629
Received September 29, 2014; accepted October 26, 2014

1 Introduction

In today's technology surfaces, interfaces and thin films are of eminent importance. The most prominent example are semiconductor devices which are solely made from thin layers or nanometer sized objects. Other examples are coatings, liquid-liquid interfaces and catalysts where chemical reactions take place at the surface. The physical and chemical properties of films and interfaces are unique and differ significantly from bulk materials. Reason is the confinement in one (in the case of a film) or more (roughness, quantum wires and dots) dimensions. The

---

***Corresponding author: Oliver H. Seeck,** Deutsches Elektronen-Synchrotron DESY, Notkestrasse 85, 22607 Hamburg Germany, e-mail: oliver.seeck@desy.de

investigation of confined systems can be done in different ways if the top surface is accessible. However, for buried layers and interfaces X-ray or equivalent neutron scattering methods are the only suitable measuring techniques which give resolution on the atomic scale, are mostly non-destructive and do not require special preparation of the sample.

The choice of X-rays or neutrons is determined by the scientific case. In general but not always, neutrons are more adequate for samples of light elements such as organic matter, the investigation of magnetism, radiation sensitive objects or in materials sciences with large samples requiring high penetration depth. X-rays are advantageous for samples containing some heavy elements (sodium and heavier), which are smaller than a few square millimeter and for measurements with very high resolution and high dynamic range.

We are concentrating on X-radiation in this article.[1] X-rays are electromagnetic waves with wavelengths of about a tenth of a nanometer. Therefore, electrical and magnetic properties of matter can be probed with this resolution. The largest detectable length scales are of the size of some ten micrometers. They are determined by the resolution function of the experiment and by the coherence properties of the X-rays. Measurements can be done time resolved. In particular cases a time resolution of around hundred pico seconds can be achieved. In future, some ten femto seconds may be attainable.

For surface near investigations different X-ray methods are available, namely X-ray reflectometry (*e. g.* [1, 2]), surface diffuse scattering methods at grazing incidence (*e. g.* [3, 4]), crystal truncation rod measurements [5] and grazing incidence diffraction (*e. g.* [6]). Each of the methods is sensitive to particular characteristics of the sample. E. g. reflectometry detects the z-dependent electron density profile whereas surface diffuse scattering is sensitive to in-plane correlation lengths and surface diffraction yields the atomic distribution close to the surface. The resulting surface near electron density or atomic distribution are not just abstract functions. In most of the cases a direct relationship to physical, chemical or materials science properties of the sample exists, such as stress, strain, surface tension or growth and catalytic parameters [7–10]. This makes surface X-ray techniques irreplaceable in surface science.

The quality of the X-ray data, and therefore the significance of the scientific results, is strongly determined by the quality of the X-ray source and the experimental setup. To satisfy the increasing request of high-end X-ray applications, in the recent decades various 3rd generation synchrotron radiation sources have been launched (*e. g.* [11–13]). They offer X-ray beams with sub-nanometer diame-

---

[1] The theory ~~for elastic scattering~~ can easily be extended to neutrons

ter, micro radian divergence and timing capabilities in the sub-nanosecond range. Moreover, the first 4th generation sources, the X-ray lasers, have become available, supplying a pulsed beam which allow for sub pico second experiments [14]. To make use of the unique features of state of the art X-ray facilities, dedicated experimental stations are available which employ specially designed X-ray detectors enabling fast data acquisition with high resolution and dynamic range.

In this article we introduce the surface sensitive X-ray methods based on diffraction, particularly reflectometry, crystal truncation rod measurements and grazing incidence diffraction. We also present two descriptive and recent scientific examples. ~~The surfaces sensitive~~ X-ray methods based on diffusely scattered beams are not presented.

2 Theory of X-ray scattering from surfaces

X-rays are electromagnetic waves. They interact with electrical charges, in case of matter mainly with the electrons. An instructive way to introduce the scattering of X-rays is to employ the Born approximation [15, 16]. For this it is assumed that the scattered intensity is small and that no energy is transfered to or from the X-ray photon. In Born approximation the scattered amplitude $A_\rho(\boldsymbol{q})$ of the X-ray waves is proportional to the Fourier transformation of the electron density $\rho(\boldsymbol{r})$ via

$$A_\rho(\boldsymbol{q}) \propto \int \rho(\boldsymbol{r}) \exp(i\boldsymbol{q} \cdot \boldsymbol{r}) d^3 r \qquad (1)$$

where the wave vector transfer $\boldsymbol{q} = \boldsymbol{k}_f - \boldsymbol{k}_i$ is the vector difference of the exit and incoming wave vectors $\boldsymbol{k}_{i,f}$. If no energy is transfered the scattering is called ‘elastic’ and $|\boldsymbol{k}_{i,f}| = k = 2\pi/\lambda$ applies where λ is the wavelength. In general, the measured quantity is not the amplitude, which is usually a complex function, but the intensity $I(\boldsymbol{q}) = A(\boldsymbol{q})A^*(\boldsymbol{q}) = |A(\boldsymbol{q})|^2$ where A^* is the conjugate complex function of A.

In the case of a single atom this scattering amplitude is called atomic form factor $F(q)$ which for $q = 0$ resembles the number of electrons. It only depends on the modulus of $\boldsymbol{q}$ as atoms are of spheric shape. The values of the form factors are accurately tabled (see [17]). Remarkably, for each atom very specific correction terms, f' and f'', exist. They are originated from direct interactions of the ~~x-ray~~ photons with the electron shells of the atom. Both, f' and f'', depend on the X-ray wavelength. They have their maximum at the element specific absorption edges with f' ~~on the~~ order of some electrons. This enables X-ray experiments with contrast variation as presented later in the example about germanium quantum huts.

TSa Please check and confirm the short running title.

Editor’s or typesetter’s annotations (will be removed before the final TeX run)

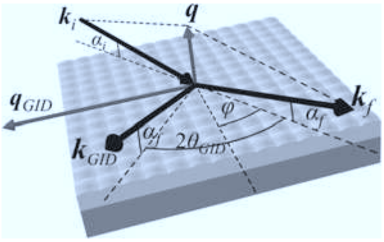

[redacted] Geometry of X-ray experiments at surfaces. The incident beam is marked by $\boldsymbol{k}_i$ with incident angle α_i. Depending on the sample orientation several exit beams may exist simultaneously. Drawn here are $\boldsymbol{k}_f$ with exit angle α_f in specular direction and $\boldsymbol{k}_{\mathrm{GID}}$ with a wave vector transfer $\boldsymbol{q}_{\mathrm{GID}}$ in the surface. The angle ϕ is the azimuth of the sample surface, the angle $2\theta_{\mathrm{GID}}$ the in-plane scattering angle.

In the context of this article, a surface is the boundary of a condensed matter sample with different electron density inside and outside. This can mathematically be expressed as $\rho(\boldsymbol{r}) = \rho_\infty(\boldsymbol{r})S(\boldsymbol{r})$ where $\rho_\infty(\boldsymbol{r})$ is the (virtual) bulk electron density extended to infinity and $S(\boldsymbol{r})$ represents the shape of the sample. In the simplest case, $S(\boldsymbol{r})$ is 1 inside and 0 outside the sample. With this representation of $\rho(\boldsymbol{r})$ and using the convolution theorem [18] the scattered amplitude can be calculated by convolving of the scattering amplitude of the infinite bulk and the surface

$$A_\rho(\boldsymbol{q}) \propto A_{\rho_\infty}(\boldsymbol{q}) \otimes A_S(\boldsymbol{q}) \tag{2}$$

where the symbol ⊗ denotes the convolution defined by

$$f(\boldsymbol{r}) \otimes g(\boldsymbol{r}) = \int f(\boldsymbol{R})g(\boldsymbol{R} - \boldsymbol{r})d^3R$$

Here, $A_S(\boldsymbol{q})$ is the scattered X-ray amplitude originated from the presence of the surface and $A_{\rho_\infty}(\boldsymbol{q})$ from an infinitely extending bulk, respectively. Consequently, the surface modifies the bulk scattering at all wave vector transfers $\boldsymbol{q}$ and vice versa the modified scattering amplitude contains information about the surface properties at all $\boldsymbol{q}$.

In principle, any surface scattering can be modeled by calculating the convolution of scattering amplitudes. However, it is more convenient to identify certain cases of surfaces sensitive scattering experiments and derive the theory separately. In the following, we discuss the crystal truncation rod scattering, the reflectivity and the grazing incidence diffraction.

2.1 Crystal truncation rods

In Born approximation, the scattering amplitude of an infinite crystal can be described as a sum of delta functions (the Bragg reflections $\delta(\boldsymbol{q} - \boldsymbol{q}_{hkl})$) which in $\boldsymbol{q}$-space are located at the Laue conditions $\boldsymbol{q}_{hkl} = h\boldsymbol{G}_a + k\boldsymbol{G}_b + l\boldsymbol{G}_c$ where h, k, l are the Miller indexes and the $\boldsymbol{G}_{a,b,c}$ are the reciprocal lattice vectors [15]. Having in mind that $\delta(\boldsymbol{q} - \boldsymbol{q}_{hkl}) \otimes A_S(\boldsymbol{q}) = A_S(\boldsymbol{q} - \boldsymbol{q}_{hkl})$, the scattering amplitude of the surface repeats at each Bragg reflection, if the reflections are sufficiently far apart. In the special case of a semi infinite sample which has the surface in the (x, y)-plane at $z = 0$, the surface scattering amplitude can be simplified as $A_S(\boldsymbol{q}) \propto \delta(q_x)\delta(q_y)A_S(q_z)$, so the X-ray amplitude from the surface scattering basically only depends on q_z which is the direction perpendicular to the surface. Convolving $A_S(\boldsymbol{q})$ with the Bragg reflections results into intensity rods along q_z. These rods are called crystal truncation rods (CTR).

To actually calculate the CTRs, the amplitudes of the single unit cells of the lattice are summed up rather than carrying out the convolution. The scattered amplitude of one unit cell of a crystal

$$S(\boldsymbol{q}) = \sum_{j=1}^{N} F_j(q) \exp(i\boldsymbol{q} \cdot \boldsymbol{r}_j)$$

is the sum of the atomic form factors $F_j(q)$ of all N atoms, taking into account the position $\boldsymbol{r}_j$ in the unit cell. $S(\boldsymbol{q})$ is called structure factor and must not be confused with $S(\boldsymbol{r})$ which is the shape function in this article. For the scattering amplitude of an infinite bulk sample

$$A(\boldsymbol{q}) = S(\boldsymbol{q}) \sum_{n_{a,b,c}} \exp(i\boldsymbol{q} \cdot [n_a\boldsymbol{a} + n_b\boldsymbol{b} + n_c\boldsymbol{c}]) \tag{3}$$

all structure factors have to be summed up, complying with the positions of the unit cells in the crystal which are given by multitudes of the lattice vectors spanning the unit cell $\boldsymbol{a}, \boldsymbol{b}, \boldsymbol{c}$.

This equation has the form of a product of three geometrical series $\sum_n x^n$ with $n = n_{a,b,c}$ and $x = \exp(i\boldsymbol{q} \cdot \boldsymbol{y})$ with $\boldsymbol{y} \in \{\boldsymbol{a}, \boldsymbol{b}, \boldsymbol{c}\}$. The calculation of the sum is rather simple in the case of finite geometrical series as a generalized formula exists [19].

In the simplest case and assuming that the lattice vector $\boldsymbol{c}$ is parallel to the z-axis, the surface information enters through the truncation of the series in (3) at some index n_{c0} which corresponds to $z = 0$. The indexes $n_{a,b}$ are of no further relevance for the CTR surface scattering as they correspond the scattering amplitudes generated along the in-plane direction. In the case of a thin layer with finite thickness d the sum starts at some other index n_{cd} with $n_{cd}c = -d$, thus, the series (3) has a finite length and can be calculated. In the case of semi-infinite samples

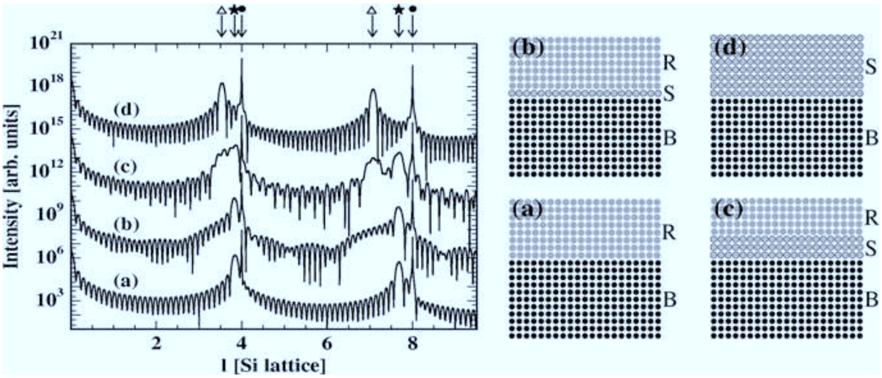

Figure 2: Left: Calculated CTRs ~~for~~ strained Germanium layers on a silicon substrate. The letters correspond to the sketches on the left. The symbols on the top mean the position of Bragg reflections: silicon (•), relaxed germanium (△), strained germanium (⋆). The q_z-axis is displayed in units of the miller index l of silicon. Curves are shifted for clarity. Right: Sketches of the corresponding samples. Bulks silicon (B), strained germanium (S), relaxed germanium (R).

the X-ray absorption factor $\exp(-z/\Lambda)$ with the absorption length Λ limits the series (3). The X-ray absorption damps the scattering amplitude from atomic layers inside the sample and all terms at z-values much larger than Λ become insignificantly small. Therefore, due to X-ray absorption the series (3) of a semi-infinite sample always becomes finite and can accordingly be calculated by means of the generalized formula for finite geometrical series.

This procedure can be applied to various surface structures. For example, for stacks of n crystalline layers prepared on a crystalline substrate (3) is used to calculated the scattered X-ray amplitude $A_j(\boldsymbol{q})$ for each layer j and the substrate separately. The total scattering amplitude is then given by the sum of all scattering amplitudes

$$A(\boldsymbol{q}) = \sum_{j=0}^{n} A_j(\boldsymbol{q}) \exp(-iq_z z_j)$$

where the phase shifts of the amplitudes due to the z_j-positions of the layers have to be taken into account.

The concept of CTRs is not only restricted to crystalline layer systems but can be extended to any surface or interface structure with preserved crystallinity. Examples are artificial nano-structures on substrates [20], surface roughness or surface reconstructions [5]. The only requirement is that all parts of the sample exhibit crystalline order.

An example is shown in Figure 2 for which an eight atomic layer thick germanium layer is positioned on top of a semi-infinite silicon substrate. For the calculation it was allowed for straining or relaxing the germanium layer in different ways. The according CTRs exhibit intensity maxima which are marked by symbols on the top of the graph. The maxima are the Bragg reflections and the positions in q-space, in the figure given in units of the Miller index l for silicon, are determined by Laue conditions of silicon, germanium and strained germanium, respectively. The width of the Bragg reflections and the oscillation periods are determined by the thickness of the according layer via $\Delta q = 2\pi/d$.

In summary, CTR measurements are a useful tool to investigate surface near crystal structures, however, they are fully insensitive to amorphous matter. In a later chapter an example is shown of CTR measurements on semiconductor multilayer films which exhibit self organized inverted quantum hut structures.

2.2 Reflectivity

As mentioned, CTRs do not occur at amorphous matter. The reason is that (3) describes the scattered X-ray amplitude of well ordered materials through the sum over unit cells. To generalize the concept of surface scattering we are starting again from (1) by locating the sample surface in the (x, y)-plane at $z = 0$. Samples of this type could be surfaces of liquids, stacks of different materials or surface near layers. For now, we are assuming full translation symmetry in the (x, y)-plane. This means that atoms are not considered. Instead, an averaged z-dependent electron density profile $\rho(z)$ is used (see Figure 3). With this information (1) becomes

$$A(\boldsymbol{q}) \propto \int_{-B/2}^{B/2} \int_{-\frac{D}{2\sin\alpha_i}}^{\frac{D}{2\sin\alpha_i}} \int_{-L_1}^{L_2} \rho(z) \exp(iq_x x + iq_y y + iq_z z) dz dy dx.$$

Here, the limits of the integration in x direction are determined by the X-ray beam width B. In the y-direction (along the beam direction) the limits are given by the footprint of the beam with height D and in z direction the limits $L_{1,2}$ are set to values well outside the sample.

In the following, only beams with wave vector transfers $\boldsymbol{q}$ parallel to the z-component are taken into account. This means, that the condition $\alpha_i = \alpha_f$ and $q_z = 2k \sin\alpha_i$ holds (see Figure 1) where $\alpha_{i,f}$ are the incident and the exit angles of the X-rays measured to the surface plane. This type of measurement is called

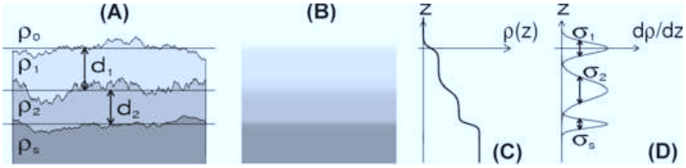

Figure 3: (A) Possible representation of a two layer system on a substrate. (B) In-plane average density generated from (A). (C) electron density $\rho(z)$. (D) derivative of (C). The values σ represent the rms-roughness values of the according distribution functions.

X-ray reflectivity. ~~Now, we can write~~

$$A(\boldsymbol{q}) \propto \delta(\cancel{q_x}) \frac{\delta(q_x)}{q_z} \int_{-L_1}^{L_2} \rho(z) \exp(iq_z z) dz$$

where the prefactor originates from the integration along the footprint direction. By concentrating on the z components this equation can be reformulated as

$$A(q_z) \propto \frac{1}{q_z^2} \int \frac{d\rho(z)}{dz} \exp(iq_z z) dz. \tag{4}$$

using the fact that X-rays are not scattered from the z-positions $L_{1,2}$ outside the sample.

Equation (4) represents the scattered amplitude in the case of an X-ray reflectivity experiment. All properties of interfaces or layer systems, such as layer thickness and interface roughness, determine the shape of the reflectivity data $A(q_z)$ via a Fourier transformation of the derivative of the electron density profile (see Figure 4). The pre-factor $1/q_z^2$ damps the scattered amplitude at large $\alpha_{i,f}$. Therefore, the normalized reflected intensity, called reflectivity, drops at least with $1/q_z^4$.

Equation (4) is very descriptive, useful and easy to use, however, there is a weak point: The assumption that the scattering signal is weak, as required for the Born approximation, is inherently wrong for small incident angles. Therefore, this equation cannot describe the full X-ray reflectivity curve. To come around this problem the reflectivity has to be calculated using the dynamical scattering theory which takes into account the full theory of electromagnetic waves. For reflectivity this means to employ the refractive index n which in the case of X-rays can be written as (*e. g.* [2])

$$n = 1 - \delta + i\beta \tag{5}$$

with

$$\delta = \frac{\lambda^2}{2\pi} r_e \rho \quad \text{and} \; \beta = \frac{\lambda}{4\pi\Lambda} \tag{6}$$

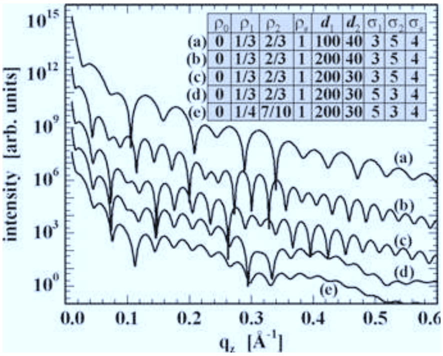

	ρ_0	ρ_1	ρ_2	ρ_s	d_1	d_2	σ_1	σ_2	σ_s
(a)	0	1/3	2/3	1	100	40	3	5	4
(b)	0	1/3	2/3	1	200	40	3	5	4
(c)	0	1/3	2/3	1	200	30	3	5	4
(d)	0	1/3	2/3	1	200	30	5	3	4
(e)	0	1/4	7/10	1	200	30	5	3	4

Figure 4: Calculated X-ray reflectivities in Born approximation for different combinations of parameters of the density profile according to Figure 3. Every single parameter significantly influences the shape of the curves. Numbers of σ and d ~~ar~~ given in Å. Curves are shifted for clarity.

and the classical electron radius $r_e = 2.81719 \times 10^{-5}$ Å. Here, effects of the electronic shell structure of atoms have been neglected. The value δ is called dispersion. It is directly proportional to the electron density ρ. The value β is called absorption depends on the absorption length Λ.

It is evident that the refractive index is smaller than unity for X-rays. Consequently, a critical angle $\alpha_c[\mathrm{rad}] \approx \sqrt{2\delta}$ exists and for $\alpha_i < \alpha_c$ total external reflection is observed. To actually calculate the reflectivity using the dynamical scattering theory the density profile has to be sliced into layers. In the case of multilayer samples this is naturally possible. In other cases, the electron density profile can be approximate by very narrow slicing virtually perfect (see Figure 5).

Having adequately sliced $\rho(z)$, which is equivalent to slice the refractive index profile $n(z)$, the Fresnel reflection coefficients

$$r_{j,j+1} = \frac{k_{z,j} - k_{z,j+1}}{k_{z,j} + k_{z,j+1}} \quad \text{with} \tag{7}$$

[redacted]

of each interface between slice j and $j+1$ are used to calculate the amplitude of the X-ray reflectivity [21]. The recursion algorithm

$$X_j = \exp(-2ik_{z,j}z_j)\frac{r_{j,j+1} + X_{j+1}\exp(-2ik_{z,j+1}z_j)}{1 + r_{j,j+1}X_{j+1}\exp(-2ik_{z,j+1}z_j)} \tag{8}$$

is employed to calculate the amplitude of the reflected beam where, actually, X_j is the ratio of the amplitudes of the reflected wave and the transmitted wave. The starting value is $X_{n+1} = 0$ as no beam is reflected from the backside of a semi-infinite sample. The recursion is carried out until $j = 1$. At the vacuum side of

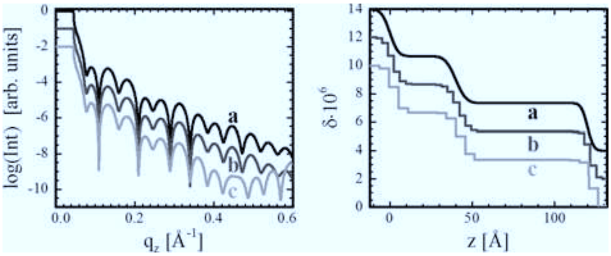

Figure 5: Left: Calculated X-ray reflectivities using the Fresnel theory according to the values of case (a) in Figure 4. The plateau of the total external reflection, originated from $n(z)$, is visible at small q_z. The three curves a,b and c correspond to differently sliced δ-profile on the right with (a) 1000, (b) 40 and (c) 25 slices. Curves of left and right ~~graph~~ are shifted for clarity.

the top interface the amplitude of the transmitted wave, which is equivalent to the incident beam, is unity, thus $X_1 = A(q_z)$ and the reflectivity is given by $|X_1|^2$. Examples of resulting reflectivity curves are displayed in Figure 5. They show the plateau of total external reflection at $q < 0.04\text{Å}^{-1}$ which has not been predicted by the Born approximation (Figure 4). For large q_z the curve strongly depends on the accuracy of the slicing. ~~It shows~~, that the step width of the slicing Δz should be smaller than $\Delta z \leq 2\pi/(4q_{z,\max})$ with $q_{z,\max}$ being the maximum q_z-value of the reflectivity.

In summary, X-ray reflectivity measurements are sensitive to the z-dependent profile of the refractive index which is proportional to the electron density. Hence, reflectivity data can be used to measure film thickness, interfacial roughness and average electron density of mulitlayer samples with accuracy on the Å level. In a later chapter an example of reflectivity data taken at mercury-electrolyte interfaces is presented which shows that layers of ions form on applying an electrical potential across the interface.

2.3 Grazing incidence diffraction

Coming back to crystalline samples it may occur that on zero incident angle α_i and and exit angle α_f the in-plane rotation ϕ of the sample surface matches the Laue condition of an in-plane lattice vector with the in-plane scattering angle $2\theta_{\text{GID}}$ (see Figure 1) [6, 22]. In this case the corresponding wave vector transfer q_{GID} would be in the surface with $q_z = 0$. However, in Born approximation this scenario is not realistic as zero incident and exit angle means that all X-ray photons actually pass the surface. On applying small $\alpha_{i,f}$ to allow for photons hitting the surface q_{GID} would ~~not the~~ Laue condition of the in-plane lattice vector and the measurement of surface near in-plane characteristics of crystals seems to be virtually impossible.

But as for X-ray reflectivity, the Born approximation is oversimplifying the reality and refraction effects have to taken into account. For this, we consider the X-ray wave inside the matter which is transmitted with an angle α_t (see Figure 6) given by Snell's law of refraction. It turns out, that α_t is always smaller than the incident angle α_i due to the real part of the refraction index of the matter which is smaller than unity, and α_t is zero for $\alpha_i \leq \alpha_c$ where α_c is the critical angle as introduced before. However, this does not mean that the X-ray amplitude inside the matter is zero. In fact, an evanescent wave with finite penetration depth ζ forms.

The penetration depth is determined by the imaginary part of the Fresnel reflection coefficient inside the matter [6] where both waves, the incident and the exiting, have to be considered. For a surface of a sample with refractive index n and $k_{z,(i,f)} = k\sqrt{n^2 - cos^2\alpha_{i,f}}$ the penetration depth is given by

$$\zeta = \frac{1}{|\Im m(k_{z,i} + k_{z,f})|} \tag{9}$$

which in the case of $\alpha_i = \alpha_f$ converts to $\zeta = 1/(2k|\Im m(\sqrt{\alpha_i^2 - 2\delta - 2i\beta})|)$, for small α_i given in radian. Here, the function $\Im m()$ denotes the imaginary part of a number. If it is assumed that the absorption β is significantly smaller than the dispersion δ, which is usually the case for photon energies larger than 10 keV, then we can finally write for the penetration depth of an evanescent wave

$$\zeta = \begin{cases} \dfrac{1}{2k\sqrt{\alpha_c^2 - \alpha_i^2}} & \text{for} \quad \alpha_i < \alpha_c \\ \dfrac{1}{2k\sqrt{\beta}} & \text{for} \quad \alpha_i \approx \alpha_c \\ \dfrac{\sqrt{\alpha_i^2 - \alpha_c^2}}{2k\beta} & \text{for} \quad \alpha_i > \alpha_c \end{cases} . \tag{10}$$

This means that ζ is on the order of some 10 Å for very small angles, between 100 and 200 Å for incident angles close to the critical angle and roughly linearly increasing with α_i for large incident angles. This is a very important finding. First, the evanescent wave traveling along the surface is useful for measuring pure in-plane characteristics of the sample. Second, depth profiling is possible by tuning $\alpha_{i,f}$ for adequate penetration depths.

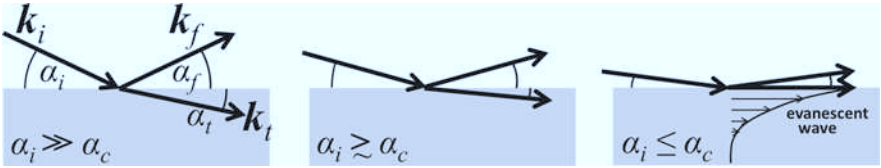

Figure 6: Incident $\boldsymbol{k}_i$, exit $\boldsymbol{k}_f$ and transmitted wave $\boldsymbol{k}_t$ with the according angles. Displayed from left to right are decreasing α_i (as noted). For α_i below the critical angle α_c an evanescent wave evolves, which exponentially decays inside the matter.

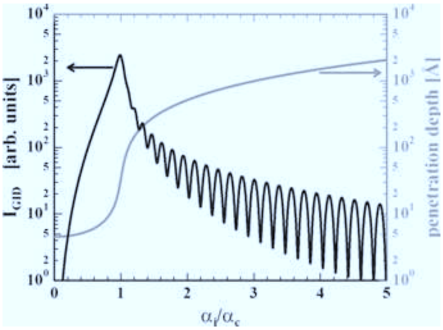

Figure 7: Intensity I_{GID} of a crystalline layer of 1000 Å thickness, calculated at $\boldsymbol{q}_{\text{GID}}$ matching the Laue condition (black curve, left axis). The surface roughness is $\sigma = 2$ Å. Also shown is the penetration depth for $n = 1 - (5 - i0.5)10^{-6}$ (gray curve, right axis).

To actually calculate the scattered X-ray amplitude from an in-plane reflection the Fresnel transmission coefficients of each layer

$$t_{j,j+1} = \frac{2k_{z,j}}{k_{z,j} + k_{z,j+1}}. \tag{11}$$

for the incident and the exiting X-ray beams are needed. Considering a sample with just one surface and no layer on top, $t_{j,j+1} = t_{0,1}$, the Distorted Wave Born Approximation DWBA yields

$$A_{\text{GID}}(\boldsymbol{q}_{\text{GID}}, q_{s,z}) \propto t_{0,1}(\alpha_i)t_{0,1}(\alpha_f)A(\boldsymbol{q}_{\text{GID}}, q_{s,z}) \exp\left(-\frac{1}{2}\sigma^2 q_{s,z}^2\right) \tag{12}$$

for the scattered amplitude of the GID reflection. Here, $\boldsymbol{q}_{\text{GID}}$ is the in-plane component of the wave vector transfer (see Figure 1) and, in good approximation, $q_{s,z} = \Re e(k_1(\alpha_f) + k_1(\alpha_i))$ is the real part of the z component of the wave vector transfer in matter (as derived from (7)), A is the scattered amplitude (see 3) and σ the surface roughness [6]. This equation generates a maximum intensity at the critical angle. Therefore, measurements are usually conducted at incident and exit angle close to the critical angle if the penetration depth is of no significance.

If a crystalline layer is investigated by GID a CTR like rod along q_z appears with oscillations according to Figure 2. In this case the penetration depth has to be considered. Reason is that for small α_i (that means small ζ) the penetration may not be sufficient to scatter X-rays from the lower interface whereas for larger α_i this is the case and intensity beatings would be observed. This is illustrated in Figure 7 which shows first the raising contrast of the beating at large penetration depths and second the maximum of the diffracted intensity at $\alpha_i = \alpha_c$

To recapitulate, grazing incidence diffraction is a method which employs the effects of the critical angle and the finite penetration depth to receive z-dependent information about in-plane crystalline structures. Examples of GID data will be shown later. There, GID has been used to solve the in-plane structure of a thin adlayer at mercury-electrolyte interfaces. This data is used to complement the reflectivity data and enables to determine the 3d structure of the interfacial layers. GID is also part of the second example where it complements CTR data to determine the strain of inverted quantum hut structures in semiconductor layers. In this example the contrast has been varied by changing the X-ray wavelength to enhance the sensitivity of the measurements.

3 Examples

In this chapter two example will be presented in more detail. The first is an investigation of layers arising at mercury-electrolyte interfaces under electrostatic potential. The second example deals with strain determination in inverted Ge-Si quantum hut structures. Both example stress on the X-ray method and the scientific outcome. Details on sample preparation will not be presented.

3.1 X-ray studies of crystal nucleation at the mercury-electrolyte interface

X-ray reflectivity and GID are complementing methods in identifying the structure of crystalline layers which, for example, appear at mercury-electrolyte interfaces on applying electrostatic potentials. One example is the work of A. Elsen et al. [23] which is summarized here.

Chemical reactions of two immiscible liquids take place at the interface. The surface area is a very well defined environment being soft, smooth, defect- and stress-free and with a well defined equilibrium state. That means that at liquid-liquid interfaces the growth of materials can occur in a very controlled way. There-

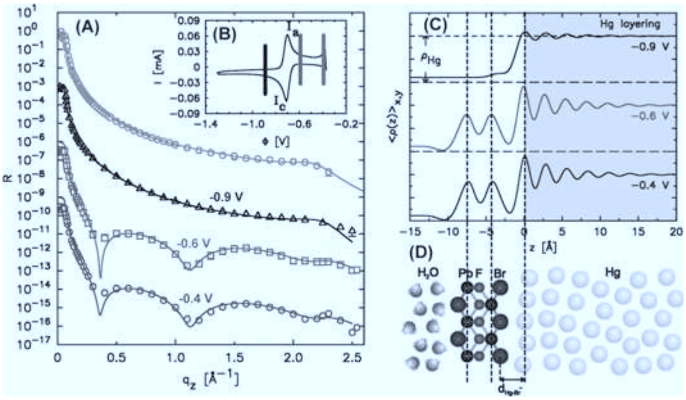

Figure 8: (A) Measured (symbols) and fitted (solid lines) X-ray reflectivities of the mercury-electrolyte interface, all shifted vertically for clarity. The upper curve is a reference without Pb^{2+} in the electrolyte. For the others the potential of ~~th~~ mercury against a reference anode is given. (B) The corresponding cyclic voltammogram with the vertical bars at the potentials of the reflectivities. (C) Electron density profiles which have been used for the fit. The reference is not shown. (D) A possible arrangement of atoms according to (C).

fore, the investigation of the contact area of two liquids is of eminent importance for material synthesis. To analyze the growth of such layers with atomic resolution, X-ray scattering methods are superior over others: They are non-destructive and do usually not affect the chemical reaction. Furthermore, full 3d information is available.

The initial stages of crystal growth at model mercury-electrolyte interfaces have been investigated with X-ray reflectivity and grazing incidence diffraction. For this the electrolyte, a sodium fluoride base electrolyte containing Pb^{2+} and Br^{-} ions has been used. The crystal growth has been controlled electrochemically via a Faradaic reaction. Pb amalgamates into Hg at potentials ≤ -0.70 V (measured against a reference electrode situated in the electrolyte), whereas at more positive potentials the amalgamated lead is released into the electrolyte. This fully reversible process can be investigated by measuring the electron density profile perpendicular to the mercury-electrolyte interface using X-ray reflectivity measurements, the in-plane structure by grazing incidence diffraction. The presented data has been recorded at the high resolution diffraction beamline P08 [24] which is situated at the 3rd generation synchrotron radiation source PETRA III in Hamburg, Germany [13].

Figure 8 presents the X-ray reflectivity measurements, the refinements and the results. It shows, that during Pb amalgamation at −0.9 V the reflectivity and therefore the interface structure is identical to that of the reference: a Pb^{2+}-free

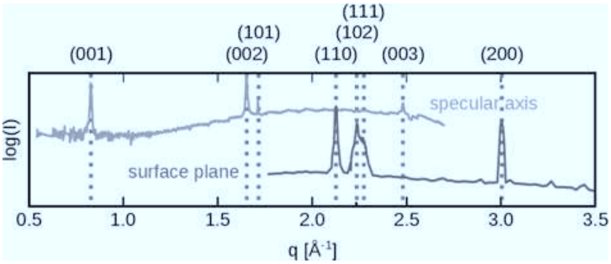

Figure 9: Measured Bragg-reflections of the PbFBr adlayer in GID geometry ("surface plane") and out of-plane data ("specular axis"). The dashed vertical lines mark the position of PbFBr Bragg-reflections. The according (hkl) is noted on top. The x-axis q denotes q_{GID} in the case if "surface plane" data and q_z in the case of "specular axis".

electrolyte on mercury. However, drastic changes are observed as the potential increases into the deamalgamation regime. Although a small maximum at $q_z \approx 2.2\,\text{Å}^{-1}$ due to Hg atomic layering still persists pronounced modulations appear in the reflectivity (Figure 8a). These indicate significant structural changes at the interface, specifically the presence of a well-defined interfacial adlayer. The period of the modulation yields an estimated adlayer thickness of 7.8 Å. The curves have been analyzed quantitatively. The modeling reveals that the density profile of the adlayer corresponds to a monolayer of PbFBr with the c-direction (the l-direction in reciprocal space) of the unit cell pointing perpendicular to the interface. This adlayer of PbFBr is composed of a stack of 5 ionic sub-layers (Figure 8c and 8d).

However, the X-ray reflectivity data does not yield any information about the in-plane structure of the adlayer, and it cannot be used as a proof for atomically ordered PbFBr films. To monitor crystallinity, in-plane GID measurements have been conducted. The positions of the Bragg-reflections which appeared in this data are a unique fingerprint and match perfectly PbFBr. For this measurement the detector has been scanned along $2\theta_{\mathrm{GID}}$ (see Figure 1) which is, for powder like samples, equivalent to scan q_{GID}. The intensity along the α_f-direction has been integrated. The data (see Figure 9 "surface plane") show the (110), (111),(102) and (200) Bragg-reflections of the tetragonal PbFBr. Surprisingly, reflections appear with Miller index $l \neq 0$, even though it was expected from the reflectivity that the l-direction of PbFBr is perpendicular to the interface meaning that only $(hk0)$ peaks would arise in the in-plane direction.

To understand this finding an out-of plane scan of the detector has been conducted with $\alpha_i = \alpha_f + \Delta\alpha$. Here, $\Delta\alpha$ is a small angular offset (of *e. g.* 0.1°) to avoid measuring the reflectivity. This data ("specular axis") is also displayed in Figure 9. The Bragg-reflection here are mainly of the type $(00l)$, as expected, but with a small contamination of the (101)-peak.

All data can be interpreted as follows: The reflectivity indicates the formation of a PbFBr adlayer with an orientation of the *c*-axis along the surface normal of the interface. The in-plane symmetry of the adlayer is identical to the a, b-plane of PbFBr and it acts as a template for 3D crystallites. The observed diffraction peaks imply the presence of these crystallites at the interface in addition to the adlayer. They are not randomly oriented but with a preferred orientation determined by the adlayer. The whole process may be viewed as a controlled precipitation, where the electrochemical deamalgamation reaction increases the Pb^{2+} concentration near the surface, promoting formation of the solid adlayer. This precursor layer acts as a template for subsequent growth of highly aligned 3D crystalline deposits.

3.2 X-ray studies of inverted quantum hut structures in a Si-Ge superlattice

CTR scattering and GID measurements have been used to determine the structure and the stress in self organized inverted quantum huts which arise when growing thin germanium silicon multilayer stacks with molecular beam epitaxy at low temperatures, as published by M. Sharma et al. [25].

Germanium and silicon crystallize in a cubic diamond structure with lattice constants $a_{\mathrm{Si}} = 5.431$ Å and $a_{\mathrm{Ge}} = 5.658$ Å. In bulk crystals Ge and Si mix perfectly at any given ratio with the resulting lattice constant $a(x)$ given by Vegard's law $a(x) = a_{\mathrm{Si}}(1 - x) + a_{\mathrm{Ge}}x$ for the composition $\mathrm{Si}_{1-x}\mathrm{Ge}_x$ [26]. However, when depositing Ge on Si (001) surfaces by molecular beam epitaxy intermixing does not occur but the growth of a well separated Ge-layer is observed (*e. g.* [27]). Due to the lattice mismatch, the first two to three layers of Ge grow heavily strained. For temperatures higher than 500 °C further growth gives rise to formation of Ge quantum hut structures. At lower growth temperatures large length-scale interdiffusion of Ge occurs into the underlying silicon provided the Ge layer thickness is between 4 and 6 unit cells [28] (see Figure 10a for a Si-Ge mulitlayer). These inverted quantum hut structures exhibit quite strong photoluminescence originated from the complex strain distribution which couples to the electronic band structure.

Subject of this investigation is the strain distribution of the inverted quantum huts. To exactly determine the strain, CTR and GID measurements have been conducted at beamline P08 at PETRA III [24] using the contrast variation method as introduced in the theory part about the atomic form factor. Accordingly, X-ray measurements have been done at two different wavelengths $\lambda_1 = 1.1227$ Å and $\lambda_1 = 1.1167$ Å where the latter corresponds the the germanium K absorption edge. For both wavelengths the atomic form factor f'_{Si} is as good as identical whereas $f'_{\mathrm{Ge},1}$ and $f'_{\mathrm{Ge},2}$ differ significantly.

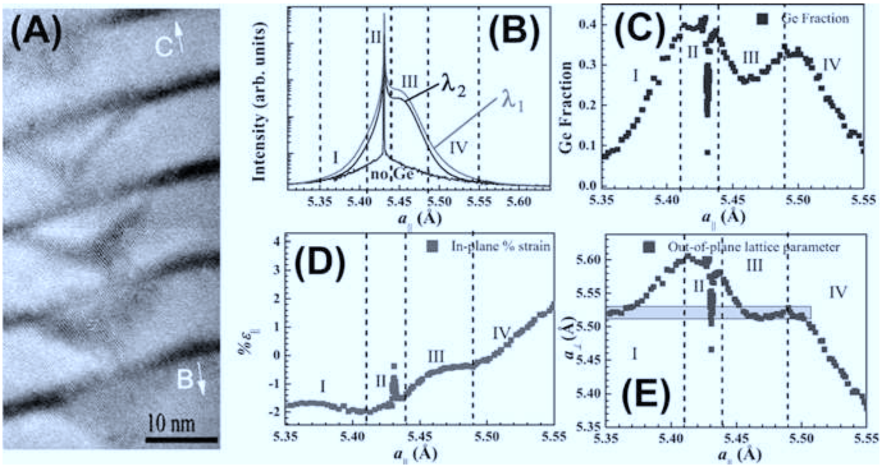

Figure 10: (A) High resolution TEM of a stack of inverted quantum huts in a Si-Ge multilayer. B and C point to the of bulk and cap layer, respectively. Dark parts correspond to high germanium content. (B) Scans around the Si 800 reflection measured in GID geometry at different wavelength and a bare reference sample. (C) Calculated fraction x of Ge, using (B) and (13). (D) In-plane strain calculated using (C), Vegard's law and (14). (E) Out of-plane lattice constant calculated using (D) and (15).

Using the equation

$$x = \left[1 + \frac{f'_{\mathrm{Ge},2}\sqrt{I_1} - f'_{\mathrm{Ge},1}\sqrt{I_2}}{f'_{Si}(\sqrt{I_2} - \sqrt{I_1})} \right]^{-1} \tag{13}$$

the content of germanium in $\mathrm{Si}_{1-x}\mathrm{Ge}_x$ can directly be determined (the small f'' corrections are neglected here) from the data $I_{1,2}$ without modeling or refinement [29]. Here, the intensities $I_{1,2}$ are measured around the Si 800 in-plane Bragg reflection by scanning the intensity ~~over~~ q_{GID} (see Figure 10b). The resulting Germanium content x is displayed in Figure 10c. Having a closer look at the figure, region II represents the $\mathrm{Si}_{1-x}\mathrm{Ge}_x$ wet layer between the actual quantum hut and the Si buffer layer as $a_{||}$ is matching $a_{\mathrm{Si}} = 5.431$ Å. The value of x is approximately 0.4 which is in accordance to the finding of the TEM picture Figure 10a which shows a diluted Ge-layer below the base of each quantum hut. Very likely, region III represents the quantum huts itself.

The in-plane strain (Figure 10e) can be derived from

$$\epsilon_{||} = [a_{||} - a(x)]/a(x) \tag{14}$$

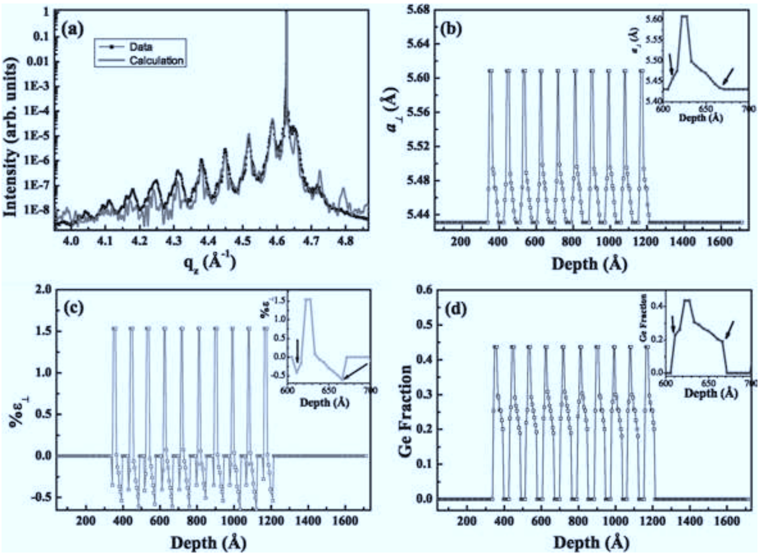

Figure 11: (a) CTR measurements at the 004 Bragg reflection. The narrow feature at $q_z = 4.63$ Å^{-1} is the Si Bragg reflection. The solid line is the refinement, the symbols ~~or~~ the data. (b) The resulting depth dependent $a_\perp(z)$. (c) The out of-plane strain as calculated from (d) and Vegard's law. (d) Ge fraction x as derived from (b) and Figure 10e and c. The insets show magnifications of one subunit of the multilayer with the arrows marking the top and bottom of the the inverted quantum hut.

when using Vegard's law and, furthermore, the out-of plane lattice constant (Figure 10e) has been derived using the Poisson relation

$$a_\perp = a(x) - \frac{C_{12}}{C_{11}}[a_{||} - a(x)]. \tag{15}$$

Here, C_{11} and C_{12} are the known values of the strain tensor where the ratios C_{12}/C_{11} for Si and Ge have similar values around 0.38.

The out of-plane lattice constant distrubution can also be deduced independently from CTR measurements (see Figure 11a). For this, the function $a_\perp(z)$ serves as the fit parameter whereas the content x of Ge has been extracted from Figure 10. The perpendicular strain can be calculated by $\epsilon_\perp = [a_\perp - a(x)]/a(x)$, corresponding to (14). The resulting $a_\perp$-profile shows the above mentioned wet layer as maxima in lattice constant and Germanium fraction. The actual quantum dot appears as a hump (see insets of Figure 11) with Ge concentrations between 20% and 30% as it was already concluded from the GID data.

From all the collected information, including the TEM picture, the average strain and lattice parameter distribution of an inverted quantum dot can be deduced. It turns out that at the base of the quantum hut the strain $\epsilon_{||}$ is almost 2% whereas $\epsilon_{\perp}$ is basically 0. On the contrary, at the tip values of $\epsilon_{||} = 0$ and $\epsilon_{\perp} = -0.5\%$ are observed. In the original publication, a further measurement was used to confirm these findings [25].

4 Conclusion

It has been shown, that X-ray reflectivity, gazing incident diffraction and crystal truncation rod measurements are sensitive tools to investigate the surface near properties of condensed matter. In particular, reflectivity measurements are suited to determine the electron density profile perpendicular to the sample surface with sub-angstrom resolution. Crystal truncation rod data and grazing incidence diffraction are useful if the sample is, at least partial, crystalline. Best results without ambiguity are achieved by combining methods, as presented in the examples. Very recent developments are stressing on time resolved surface measurements with resolution of better $1/10\,\mathrm{s}$ per full CTR-scan to investigate the reaction process on catalytic surfaces [10] or with nanosecond resolution in pump-probe mode to learn about the vibrational modes of lipid membranes [30]. This opens new perspectives for surface sensitive X-ray scattering methods.

References

1. J. Daillant and A Gibaud, *X-Ray and Neutron Reflectivity*, SpringerTS^{b} (2009).
2. M. Tolan, *X-Ray Scattering from Soft-Matter Thin Films*, Springer Tracts in Modern Physics, Vol. 148, SpringerTS^{b} (1999).
3. S. K. Sinha, E. B. Sirota, S. Garoff, and H. B. Stanley, Phys. Rev. B **38** (1988) 2297.
4. G. Renaud, R. Lazzari, and F. Leroy, Surf. Sci. Rep. **64** (2009) 255.
5. I. K. Robinson, Phys. Rev. B **33** (1986) 3830.
6. H. Dosch, *Critical Phenomena at Surfaces and Interfaces*, Springer Tracts in Modern Physics, Vol. 126, SpringerTS^{b} (1992).
7. M. E. Fitzpatrick and A. Lodini, *Analysis of Residual Stress by Diffraction using Neutron and Synchrotron Radiation*, ~~Routledge, Taylor and Francis Group~~TS^{b} (2003).
8. A. Braslau, P. S. Pershan, G. Swislow, B. M. Ocko, and J. Als-Nielsen, Phys. Rev. A **38** (1988) 2457.
9. H. Zabel and I. K. Robinson, *Surface X-Ray and Neutron Scattering*, SpringerTS^{b} (1991).
10. J. Gustafson, M. Shipilin, C. Zhang, A. Stierle, S. Hejral, U. Ruett, O. Gutowski, P.-A. Carlsson, M. Skoglundh, and E. Lundgren, Science **343** (2014) 758.
11. R. Haensel, Rev. Sci. Instrum. **63** (1992) 1571.
12. D. E. Moncton, E. Crosbie, and G. K. Shenoy, Rev. Sci. Instrum. **60** (1989) 1403.

TS^{b} Please add place of publication.

Editor's or typesetter's annotations (will be removed before the final TeX run)

13. H. Franz, O. Leupold, R. Röhlsberger, S. V. Roth, O. H. Seeck, J. Spengler, J. Strempfer, M. Tischer, J. Viefhaus, E. Weckert, and T. Wroblewski, Synchrotron Radiation News **19** (2006) 25.
14. M. Trigo, M. Fuchs, J. Chen, M. P. Jiang, M. Cammarata, S, Fahy, D. M. Fritz, K. Gaffney, S. Ghimire, A. Higginbotham, S. L. Johnson, M. E. Kozina, J. Larsson, H. Lemke, A. M. Lindenberg, G. Ndabashimiye, F. Quirin, K. Sokolowski-Tinten, C. Uher, G. Wang, J. S. Wark, D. Zhu, and D. A. Reis, Nat. Phys. **9** (2013) 790.
15. B. E. Warren, *X-Ray Diffraction*, Dover PublicationsTS^{b} (1990).
16. J. Als-Nielsen and D. McMorrow, *Elements of Modern X-Ray Physics*, John Wiley & SonsTS^{b} (2001).
17. U. Shmueli, *International Tables for Crystallography Volume B: Reciprocal space*, International Union of Crystallography,TS^{b} (2010).
18. R. N. Bracewell, *The Fourier Transform and its Applications*, Mc Graw-Hill,TS^{b} (2000).
19. M. Abramowitz and I. Stegun, *Handbook of Mathematical Functions*, ~~Dover,~~TS^{b} (1972).
20. U. Pietsch, V. Holý, and T. Baumbach, *High Resolution X-Ray Scattering: From Thin Films to Lateral Nanostructures*, SpringerTS^{b} (2004).
21. L. G. Parratt, *Phys. Rev.* **95** (1954) 359.
22. N. Bernhard, E. Burkel, G. Gompper, H. Metzger, J. Peisl, H. Wagner, and G. Wallner, Z. Phys. B Con. Mat. **69** (1987) 303.
23. A. Elsen, S. Festersen, B. Runge, C. Koops, B. Ocko, M. Deutsch, O. Seeck, B. Murphy, and O. Magnussen, P. Natl. Acad. Sci. USA **110** (2013) 6663.
24. O. H. Seeck, C. Deiter, K. Pflaum, F. Bertram, A. Beerlink, H. Franz, J. Horbach, H. Schulte-Schrepping, B. M. Murphy, M. Greve, and O. Magnussen, J. ~~Synchrotron,~~ Radiat. **19** (2012) 39.
25. M. Sharma, M. Sanyal, B. Satpati, O. Seeck, and S. K. Ray, Phys. Rev. B **89** (2014) 205304.
26. A. R. Denton and A. W. Ashcroft, Phys. Rev. A **43** (1991) 3161.
27. J. Tersoff, Phys. Rev. B **43** (1991) 9377.
28. F. Lui, F. Wu, and M. G. Lagally, Chem. Rev. **97** (1997) 1045.
29. T. U. Schülli, J. Stangl, Z. Zhong, R. T. Lechner, M. Sztucki, T. H. Metzger, and G. Bauer, Phys. Rev. Lett. **90** (2003) 066105.
30. T. Reusch, F. J. R. Schülein, J. D. Nicolas, M. Osterhoff, A. Beerlink, H. J. Krenner, M. Müller, A. Wixforth, and T. Salditt, Phys. Rev. Lett. **113** (2014) 118102.